Aeroacoustic Test Cases

L. Koloszar[1], N. Villedieu[1], H. Deconinck[1], I.S. Bosnyakov[2], S.V. Mikhaylov[2], A.N. Morozov[2], V.Y. Podaruev[2], A.I. Troshin[2], V.V. Vlasenko[2], A.V. Wolkov[2], P. Eliasson[3], T. Bolemann[4], and F. Chalot[5]

[1] von Karman Institute for Fluid Dynamics, B-1640, Rhode-St-Genese, Belgium
lilla.koloszar@vki.ac.be
[2] Central Institute of aero- and hydrodynamics (TsAGI), Zhukovsky, Russia
andrey.wolkov@tsagi.ru
[3] The Swedish Defense Research Agency (FOI), SE-164 90 Stockholm, Sweden
peter.eliasson@foi.se
[4] University of Stuttgart, Germany
bolemann@iag.uni-stuttgart.de
[5] Dassault Aviation, Cedex 300, 92552 Saint-Cloud Cedex, France
frederic.chalot@dassault-aviation.com

Abstract. In this article, the results of aeroacoustic cases obtained by high-order methods are presented. One internal and one external case are considered. The internal case is a transonic cavity. It has been computed by three parters, namely FOI-LiU (Linköping University), University of Stuttgart (USTUTT) and Dassault Aviation (DASSAV). FOI-LiU has computed with their higher order accurate finite difference solver using a block structured grid. Comparisons are made to reference calculations using an unstructured grid with Edge. USTUTT uses a high order discontinuous Galerkin spectral element code for the final high-order computations and a mixed modal/nodal DG code for the baseline computations. Dassault Aviation uses their in-house stabilized finite element code Aether, both for the reference and the higher-order computations. In both instances unstructured tetrehedral grids are used. The external case is a quasi-two dimensional generic wing and flap configuration defined in the VALIANT FP7 project. Two institutions were involved in the high-order simulation of this low-Mach number test case, $M = 0.15$, Central Institute of Aero- and Hydrodynamics, TsAGI, and the von Karman Institute, VKI. In the following, the acoustic predictions corresponding to the two test cases will be described.

Keywords: CFD, CAA, hybrid method, higher order.

1 Introduction

Flows over an open cavity may arise over the under-carriage wheel well and over an embedded weapon bay during the store release operation of a military aircraft. The acoustic tones for open cavity flows are interpreted as a consequence of the interaction between the shear layer that bridges the cavity and the aft

N. Kroll et al. (eds.), *IDIHOM: A Top-Down Approach*, Notes on Numerical Fluid Mechanics and Multidisciplinary Design 128, DOI: 10.1007/978-3-319-12886-3_29

cavity wall on which the shear layer impinges. A better understanding and prediction capability of this type of flow is of practical importance to improve the design methodology and to avoid possible flow-induced operation problems in aeronautic applications. Three partners consider the test case with turbulent flow over a rectangular cavity. FOI and USTUTT are performing hybrid RANS/LES calculations without a subgrid-scale model. Dassault Aviation is using a zonal DES (ZDES) approach.

During aircraft approach and landing, a significant portion of noise is generated by the high-lift devices. Reducing the noise during landing is very important for the comfort of the residents living nearby an airport. The airframe noise during take-off maneuver is less important, since the slope of the take-off is much steeper, and the engines are in full trust, louder than any other component. Among the various noise sources during approach and landing, the landing gear, leading-edge slat and the side edges of the flap where identified as the main airframe noise sources. The current test case considering a generic wing and flap, more precisely the noise propagation around such geometry. Two partners, namely TsAGI and VKI were contributiong to this industrial demonstrator test case. VKI used the Large-Eddy Simulation performed within the VALIANT project as noise sources while TsAGI injected stochastic perturbations in order to represent the effect of the turbulent flow.

2 Transonic Cavity Case

The test case is denoted Test Case A15 within IDIHOM and is a test case with transonic flow over a rectangular cavity; it is also known as M219 in the literature. This test case is suitable for LES or hybrid RANS/LES calculations due to the turbulent fluctuations over the cavity. Experimental, time dependent data exist on the cavity walls and ceiling and are available for IDIHOM. This test case has been measured and computed in the past with many references available, e.g. [1]– [3]. Several different cavity geometries exist; the one used in IDIHOM is the cavity with 5:1:1 length-to-depth-to-width relation. The geometry as well as the locations of the pressure probes are reproduced here in Figure 1.

The free stream values are

$$M_\infty = 0.85;\ Re = 6.8 \times 10^6 \tag{1}$$

where the Reynolds number is based on the cavity length (20 inches).

2.1 Computational Domains and Grids

FOI-LiU. For the higher order calculations with the finite difference solver Essense, calculations were carried out on a flat plate where the cavity is embedded on the flat plate. A two block structured grid was created for these calculations

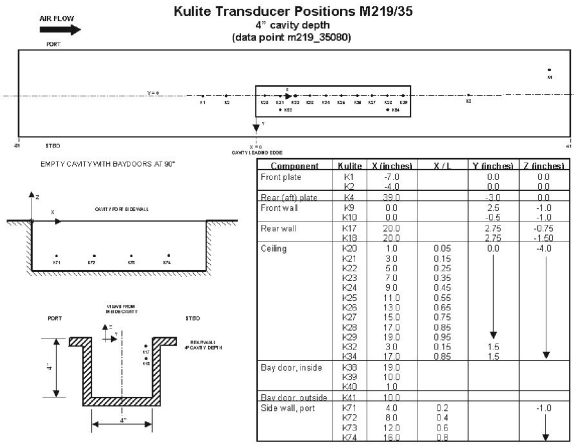

Component	Kulite	X (inches)	X / L	Y (inches)	Z (inches)
Front plate	K1	-7.0		0.0	0.0
	K2	-4.0		0.0	0.0
Rear (aft) plate	K4	33.0		-3.0	0.0
Front wall	K9	0.0		2.5	-1.0
	K10	0.0		-0.5	-1.0
Rear wall	K17	20.0		2.75	-0.75
	K18	20.0		2.75	-1.50
Ceiling	K20	1.0	0.05	0.0	-4.0
	K21	3.0	0.15		
	K22	5.0	0.25		
	K23	7.0	0.35		
	K24	9.0	0.45		
	K25	11.0	0.55		
	K26	13.0	0.65		
	K27	15.0	0.75		
	K28	17.0	0.85		
	K29	19.0	0.95		
	K32	3.0	0.15	1.5	
	K34	17.0	0.85	1.5	
Bay door, inside	K39	19.0			
	K38	10.0			
	K40	1.0			
Bay door, outside	K41	10.0			
Side wall, port	K71	4.0	0.2		-1.0
	K72	8.0	0.4		
	K73	12.0	0.6		
	K74	16.0	0.8		

Fig. 1. Cavity geometry, experimental setup and location of the pressure probes recording unsteady pressure fluctuations

where one block is located inside the cavity. To have a single boundary condition per block side, the block on top of the cavity block was split up resulting in 10 blocks all together. For the reference calculations with Edge [4], FOI-LiU has computed on two different grids, one hybrid unstructured grid that has been generated by EADS and contains a grid over the cavity, the device on which the cavity is integrated and the entire test section of the wind tunnel. The other grid is a structured grid generated by FOI-LiU over the cavity and a limited domain of the flat plate outside of the cavity, very similar to the structured grid. The structured grid is displayed in Figure 2 and the main data are summarized in Table 1.

Table 1. Details of FOI-LiU computational grids for A15 Cavity

Grid	Solver	# vol. nodes	# boundary nodes in cavity	# volume nodes in cavity	Near wall distance
Structured	Essense	2.6×10^6	41×10^3	0.73×10^6	1.2×10^{-5} m
EADS grid	Edge	6.2×10^6	77×10^3	2.0×10^6	4.0×10^{-6} m
FOI grid	Edge	1.2×10^6	16×10^3	0.5×10^6	4.0×10^{-6} m

USTUTT. The mesh used for the cavity computations by the University of Stuttgart is a modified version of the mesh provided by FOI. The mesh contains about 62,000 elements, of which about 50% are placed either inside the cavity or at a distance of less then 0.2D to the cavity. In the flat plate region the effective y^+, ($y^+ = y_1^+/(P+1)$) has been chosen to be 10, considering the schemes sub cell

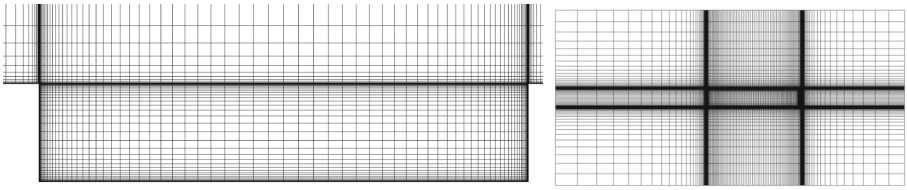

Fig. 2. Mesh of the cavity test case by FOI-LiU using Essense

resolution. Here y_1^+ denotes the height of the first grid cell and P the polynomial degree. The magnitude of y^+ could be confirmed by the computations. The mesh is displayed in Figure 3.

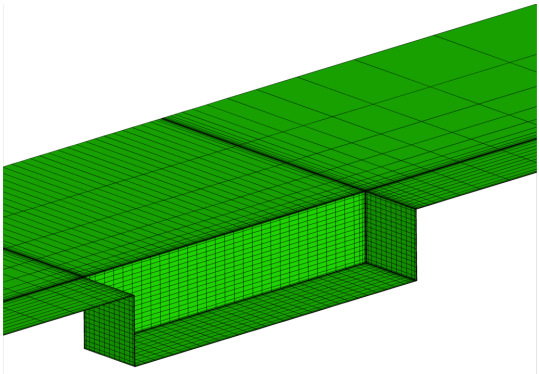

Fig. 3. Cavity mesh used by USTUTT, cut at plane through the right wall

DASSAV. Contrary to the other two contributors, Dassault Aviation has computed the M219 cavity in a configuration close to its original experimental setup, as can be seen in Figure 4. The Reference linear mesh used by Dassault Aviation is an unstructured tetrahedral mesh build on top of a triangular surface mesh with a characteristic edge size of 2 mm. In the boundary layer, the mesh is constructed with a first layer of elements of 10 μm height and a growing ratio of 1.25. In the mixing layer, an unstructured block of tetrahedra with edge lengths od 2 mm in the x and y directions and 2.5 mm in the z direction is inserted. The grid contains slightly less than 3.4 million grid points. Higher order grids are generated by adding degrees of freedom to a coarse P1 grid. The difficulty is to build a "skeleton" grid which is coarse enough to yield higher-order grids with a controlled number of grid points and still preserve the qualities in geometric representation, point density, and element distorsion of the original reference grid. Fortunately for this test case, all surfaces of the model are flat which alleviates the issue of curving the elements in the volume. A discussion about this aspect of higher-order grid generation can be found in the A04 Generic Falcon Test Case in the External Aerodynamic Test Case section [5] and also in Chapter II.2

in the section dedicated to the numerical method developed by DASSAV [6]. With these constraints, the skeleton P1 mesh built on a different surface grid with a characteristic edge size of 4 mm could not be made coarser than about 450,000 grid points; consequently the corresponding P2 grid (and the matching P1 grid) contains 3.5 million grid points. Coarsening techniques developed later on for the A04 Falcon test case could probably have been similarly applied to the cavity to produce yet coarser higher-order grids [5].

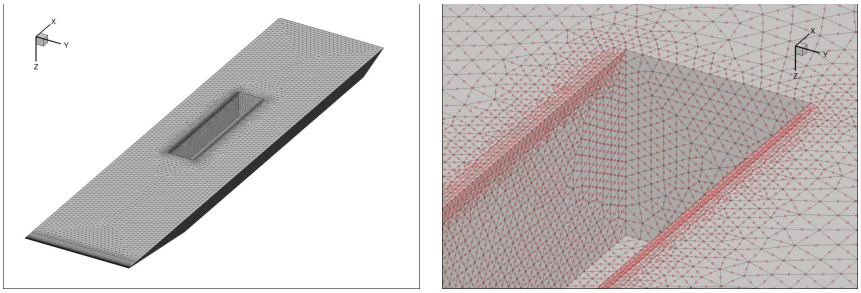

Fig. 4. Configuration and surface view of the P2 mesh used by DASSAV

2.2 Numerical Methods, Reference and Higher-Order Solutions

FOI-LiU. For the higher order accurate calculations FOI-LiU use the finite difference solver Essense that has been further developed and validated within IDIHOM. The higher order code is based on Summation By Parts (SBP) combined with Simultaneous Approximation Term (SAT) approach with penalty terms that guarantee accuracy and stability [7], [8]. The code is able to handle arbitrary order of spatial accuracy, currently limited to 5^{th} order. The code uses explicit time stepping with a 4^{th} order accurate additive Runge-Kutta scheme.

The unsteady calculations were initiated from poorly converged steady state calculation with local time steps. The intention was to use the same hybrid RANS/LES model as in Edge. For this purpose this algebraic model has been implemented in Essense. In the calculations, however, the model imposed a severe restriction on the time step due to small cells away from the wall caused by the H-topology of the employed mesh. This model was therefore abandoned and the calculations presented here have been computed without a model. Only one calculation was completed during IDIHOM. This calculations employs a scheme that is 4^{th} order accurate in the interior, 2^{nd} order accurate at the boundaries making it globally 3^{rd} order accurate. Adiabatic weak wall boundary conditions were used inside the cavity and on the flat plate. Far field characteristic boundary conditions were used elsewhere. The higher order calculation progress for about 60 through flows, the solutions from last 40 through flow are used for the statistics.

The reference calculations for this test cases were carried out some time ago and have been repeated for IDIHOM. The 2^{nd} order backward difference implicit

method is used in time which is A-stable, i.e. stable for all sizes of physical time step. In dual time multigrid with 3 levels accelerate the convergence. The calculations progress for about 120 through flows, i.e. L/U_∞, where L is the cavity length and U_∞ is the free stream velocity. Some computational parameters are given in Table 2.

Table 2. Sizes of time steps and number of inner iterations for the reference cavity calculations

Grid	Solver	Δt	Δt per T	N inner iterations
Structured	Essense	1.0×10^{-8}	182×10^3	1
EADS grid	Edge	2.0×10^{-5}	91	32
FOI grid	Edge	1.0×10^{-5}	182	40

In Figure 5 the overall the sound pressure level (SPL) and the overall sound pressure level (OASPL) are displayed and compared to experimental values. The higher order results compare reasonably well to the experimental values of SPL. The main tonal peaks are captured. The higher order results have a tendency to have somewhat larger amplitudes of the oscillations compared to the reference results. This may be due to the lack of RANS/LES model for the higher order calculations or possibly a too short and coarse sampling interval. The OASPL is obtained by integrating SPL for all frequencies. The computed OASPL from the higher order scheme and from the reference calculations with the EADS grid agree best with the experimental values, the over prediction of OASPL is common.

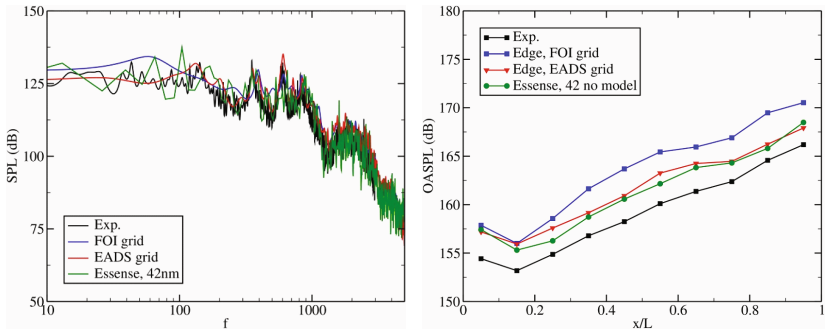

(a) SPL at kulits k21, $x/L = 15\%$ (b) OASPL

Fig. 5. Local and Overall Sound Pressure Level by FOI-LiU

USTUTT. USTUTT computed baseline higher order computations for the cavity testcase within the ADIGMA project [9] computed with USTUTTs mixed

modal/nodal hp-adaptive DG code HALO. The calculations were carried out for a different Reynolds number (Re=2×10^5) and have hence been left out here.

The cavity computations have been performed using the high order discontinuous Galerkin spectral element code Flexi developed by the Numerical Research Group (NRG) at the University of Stuttgart [10]. A polynomial degree of $P = 4$ has been chosen for the computations. For the computation a model-free approach has been chosen, however an incomplete polynomial de-aliasing has been applied using over integration. The de-aliasing reduces unphysical oscillations of the solution and thus provides 'clean numerics' and in our case also significantly reduces destabilizing effects caused by the high Reynolds and Mach number. For the overintegration a polynomial degree of $P_{Over} = 6$ has been chosen, which was regarded as a good compromise between speed and accuracy, where full overintegration would require $P_{Over} = 9$. During the computation occasionally occurring shocklets have been observed, therefore a low amount of artificial viscosity has been used to provide additional stability. The amount of artificial viscosity has been controlled by a Persson-type modal pressure indicator. Compared to the baseline results, only 20% of the amount of artificial viscosity was sufficient for this computation.

For the time discretization USTUTT has employed a 4^{th} order explicit Runge-Kutta scheme. The average time step of the simulation was typically in the range between $\Delta t = 1.4 \times 10^{-7} - 1.6 \times 10^{-7}$. The data at the Kulites was collected every 4^{th} time step, resulting in a very high sampling rate of about 1.6 Mhz. From $t = 0.0s - 0.035s$ the polynomial degree has been gradually increased from $P = 2$ with an increased amount of artificial viscosity to the final simulation setup with $P = 4$. The collection of the data started at t=0.05s, which equals to 27 through-flows. The total averaging time was 0.11s being about 60 through-flows.

The domain has been chosen to be periodic in spanwise direction. For the flat plate and the cavity itself adiabatic no-slip boundary conditions have been applied. At the inflow and the top characteristic conditions have been used, producing a boundary layer thickness of 0.1D at the cavity leading edge, to have comparable results to the which is identical to the results by Chen et al. [1]. At the outflow characteristic non-reflecting boundary conditions have been applied.

The overall computation contains 7.7×10^6 DOFs, with an additional 13.4×10^6 DOFs used for the de-aliasing. The simulation has been carried out on the Cray XE6 cluster Hermit at HLRS in Stuttgart with on 4096 cores. The number of DOFs/core was about twice the number of which the code reaches its peak efficiency (2000-3000 DOFs/core), more cores could not be used for availability reasons on the cluster.

For the evaluation of our computations we compare the sound pressure level spectra and the overall sound pressure level along the Kulites K20-K29 placed equidistantly in streamwise direction on the cavity ceiling, the results on one of the Kulites is displayed in Figure 6.

The plots of the sound pressure level reveal that all cavity modes are predicted slightly too high in frequency, while the amplitude prediction differs somewhat

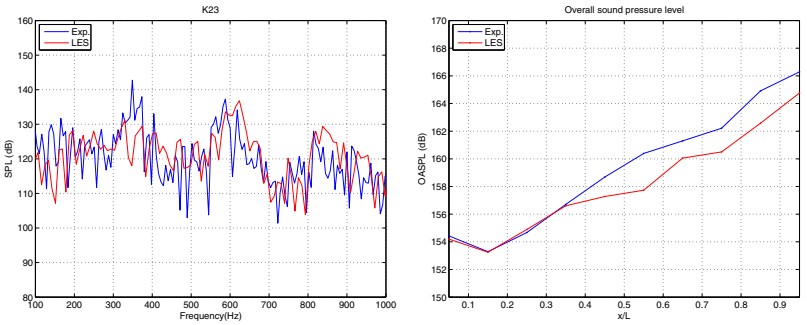

(a) SPL at kulits k23, $x/L = 35\%$ (b) OASPL

Fig. 6. Local and Overall Sound Pressure Level by USTUTT

between the Kulites. It is clearly visible, that the 3^{rd} and 4^{th} mode are predicted best by the LES computation, with respect to both frequency and amplitude. Even some of the higher modes are well resolved, which can be best seen at Kulite 23. The predictions for the first mode suffer from the relatively short averaging time compared to the experiment. To fully capture this mode a largely longer averaging time would be required. Nevertheless both amplitude and frequency prediction are in an acceptable region. The SPL for the 2^{nd} mode can be regarded too low for some Kulites, for others the 2^{nd} mode is nearly missing. While the reason for this behaviour is unknown, many simulations from literature suffer from the same problem e.g. [2]. The SPL prediction at Kulites 20-23 at the beginning of the cavity matches the experimental results somewhat better, compared to the Kulites at the end. In an overall view the mode prediction is satisfying, with exception of the 2^{nd} mode.

Table 3. Modal frequency and amplitude at K29, results from USTUTT

Mode	1	2	3	4	5
Rossiter	159 Hz	371 Hz	582 Hz	794 Hz	1005 Hz
Experiment	150 Hz	350 Hz	590 Hz	810 Hz	991 Hz
	142 dB	153 dB	146 dB	135 dB	129 dB
LES-N4	190 Hz	380 Hz	623 Hz	840 Hz	1010 Hz
	140 dB	140 dB	145 dB	137 dB	127 dB

Regarding the overall sound pressure level the computations do in general match the experimental results very well as displayed in Figure 6. Especially in the first 3^{rd} of the cavity the OASPL is nearly identical to the measured results. In the region near $x/L = 0.4$ where the pressure oscillations caused by the shear layer reach their maximum the results start to slightly diverge up to a maximum

difference of 3 dB, which then decreases again to 1-2 dB difference till the end of the cavity.

DASSAV. For all computations, Dassault Aviation used its industrial stabilized finite element code `Aether`. It relies on *continuous* isoparametric Lagrange polynomials of any order computed on unstructured grids as finite element shape and trial function spaces (solutions are C^0 continuous and the same degree of interpolation is used for both the solution variables and the space coordinates). So far, only tetrahedral elements have been implemented in 3-D up to P3. More details about the numerical method and its higher-order implementation can be found in [6].

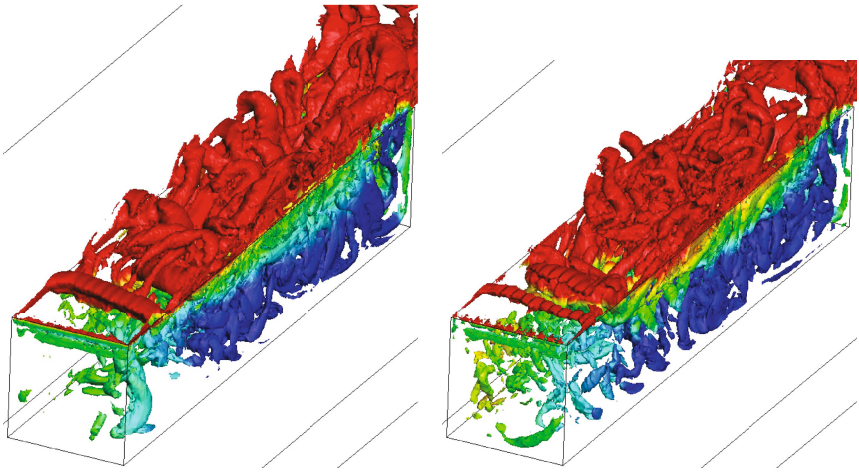

Fig. 7. Turbulent structures in the QinetiQ M219 cavity computed by DASSAV: standard 2nd-order linear P1 elements (left) vs. 3rd-order quadratic P2 elements (right).

For unsteady calculations fully implicit time integration with dual time stepping is performed based on the standard second-order Gear's scheme. The same time step of 1.5×10^{-5} s (that is 121 time steps per through flow over the cavity length) is used for all computations whatever the order of the space integration. Third order calculation may suffer from a time integration which is only second order accurate. Our experience with DES calculations and in particular with this test case tells that time accuracy should be sufficient with such a time step. The effect of a time step reduction is shown in section [6]. Nevertheless, keeping everything equal, including the time integration scheme, enables a fair comparison between 2nd and 3rd order spatial accuracy.

For all simulations, the flowfield is initialized with a steady RANS computations using the Spalart-Allmaras turbulence model. The computation is pursued in a unsteady mode with a Zonal DES approach [11]. After a settling time of 195 ms, unsteady data is acquired for another 225 ms, which accounts for a total

simuation time of 420 ms (i.e., 230 through flows). 186 ms are post-processed to produce the energy spectra and the OASPL curves. For a better comparison, especially at low frequencies, the experimental pressure history is post-processed over the same time interval. All calculations were performed on 1024 cores of an IBM BlueGene/P.

In Figure 7, isovalues of the Q-criterion colored by the Mach number are presented for the 2nd-order linear P1 and the 3rd-order quadratic P2 solutions computed on nested grids and thus containing the same number of degrees of freedom. The higher-order simulation transitions sooner to full 3-D turbulence and contains much finer turbulent structures.

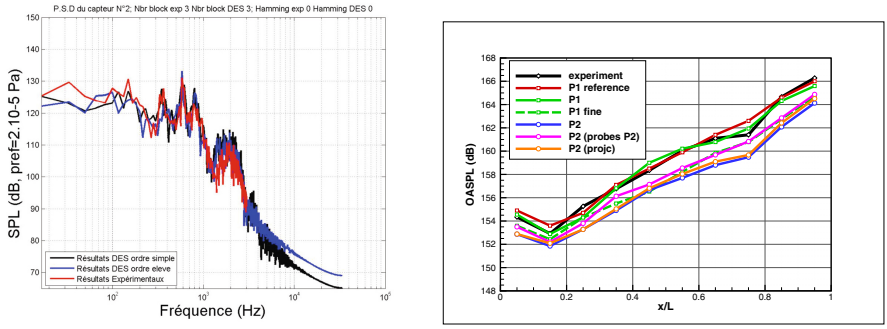

(a) SPL at Kulite K21, $x/L = 15\%$ (b) OASPL

Fig. 8. Local and Overall Sound Pressure Level by DASSAV

A typical SPL frequency spectrum corresponding to Kulite #21 is displayed in Figure 8a. It shows a reasonable agreement between the experiment (in red) and the different simulations both in terms of Rossiter peak locations and amplitude. One must note that the higher-order solution (in blue) exhibits more energy in the higher part of the spectrum.

In Figure 8b, OASPL plots corresponding to different realizations of the simulation are presented. The red and green curves represent respectively the Reference solution and the P1 solution computed with the same degrees of freedom as the higher-order solutions. Both solutions are quite similar and are in good agreement with the experiment shown in black (a few tenth of a dB on the average, see Table 4). Note that the Reference solution corresponds to a longer simulation time of 350 ms. This confirms that the statistics are converged for the newer computations which account for simulations times of 225 ms. The P2 third-order solution is plotted in blue. It shows a drop in OASPL 1 to 2 dB below the experiment. We believe that the more precise P2 computation reveals some of the limitations of the underlying Smagorinsky subgrid scale model in the DES. A finer P1 simulation, shown in a green dashed line, exhibits the same tendency of decreased OASPL's; the corresponding mesh is the same as the P1 and P2 meshes, except in the cavity region where the typical grid size has been

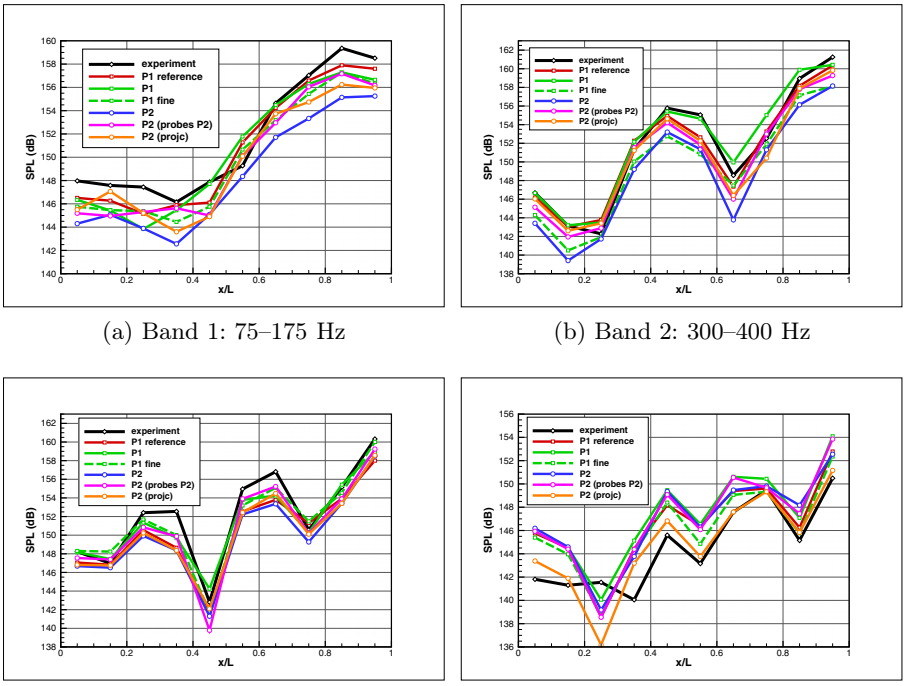

(a) Band 1: 75–175 Hz

(b) Band 2: 300–400 Hz

(c) Band 3: 550–650 Hz

(d) Band 4: 750–850 Hz

Fig. 9. Band-integrated Sound Pressure Levels by DASSAV

reduced from 2 to 1 mm; this mesh contains close to 3.9 million grid points. A more detailed discussion about the effects of mesh refinement, subgrid scale model, time step and scheme order can be found in [6].

Finally, two additional curves are presented in Figure 8b. For the sake of simplicity, earlier higher-order computations were carried out with the same sampling routine as P1 computations, that is the pressure signal was linearly interpolated at the location of the experimental Kulites. The effect of the actual higher-order interpolation is shown in the pink curve. Depending on the pressure tap, an increase of up to 1 dB is observed in OASPL, bringing the higher-order P2 results very close to the refined mesh P1 results. This stresses the importance of postprocessing higher-order solutions with adapted higher-order techniques. This remark is also valid for line and contour plots. The orange curve in Figure 8b represents the effect of the second order Navier-Stokes derivatives in the SUPG/GLS stabilization term of DASSAV residual-based stabilized finite element code. This term is zero for 2nd-order linear solutions and was dropped so-far for higher-order computations. The effet is not so sensitive on OASPL's but is more significant at certain frequencies as can be seen in the band-integrated SPL's in Figure 9. Frequency bands are defined for this test case according to the analysis of Larchevêque [12]. Again, the difference in SPL with respect to

the orginal P2 solution is significant, and the experimental level can even be retrieved for the higher frequency band. Unfortunately, the combination of both higher-order interpolation for pressure probes and of the higher-order term in the stabilization could not be tested during the duration of the project.

The band-integrated sound pressure levels (SPL's) in Figure 9, plotted in the same colors as the OASPL's, show that the main physics is captured in all simulations over the complete range of frequencies. As could be anticipated, higher frequencies are better captured on P1 refined meshes and higher-order solutions with the best numerical ingredients. More on that aspect can be found in [6].

2.3 Assessment of High-Order Solutions

In an attempt to quantify the deviation from the experimental OASPL and to make a cross comparison between partners results we define the normalized deviation D as

$$D = \frac{\parallel O_{CFD} - O_{exp} - \overline{\delta O} \parallel_2}{\overline{O}_{exp}} = \frac{\sqrt{\frac{1}{N}\sum_{i=1}^{N}(O_{i,CFD} - O_{i,exp} - \overline{\delta O})^2}}{\overline{O}_{exp}} \tag{2}$$

$$\overline{\delta O} = \frac{1}{N}\sum_{i=1}^{N}(O_{i,CFD} - O_{i,exp}) \tag{3}$$

and where $\overline{O}_{exp} = 159.2dB; N = 10$. The intention with the derived formula for the deviation is to define a measure that gives a zero value if the shape of OASPL is identical to the shape of the experimental OASPL. It allows for a shift in absolute level though.

In Figure 10 the OASPL by FOI-LiU, USTUTT, and DASSAV using HOM are displayed. In Table 4 below we give the deviation for the different calculations. The deviation obtained by FOI-LiU between the higher order and reference results is very similar indicating that the two solutions follow experimental OASPL equally well. The slightly higher deviation obtained by USTUTT is due to the

Table 4. Computed deviation to experimental values

Partner	Solution	D	$\overline{\delta O}$ (dB)
FOI-LiU	Reference EADS grid, 2^{nd} order	3.0×10^{-3}	2.480
FOI-LiU	HOM, 3^{rd} order	3.0×10^{-3}	2.077
USTUTT	Flexi, 5^{th} order	5.4×10^{-3}	-1.027
DASSAV	Aether, Reference, 2^{nd} order	3.1×10^{-3}	0.200
DASSAV	Aether, 2^{nd} order	3.0×10^{-3}	-0.074
DASSAV	Aether, 3^{rd} order	2.7×10^{-3}	-1.936

fact that their shape deviates somewhat more from the shape of the experimental results although there is a very good experimental match upstream in the cavity. In the case of DASSAV, both 2nd-order solutions present similar deviations; the 3rd-order simulation produces however a slightly lower deviation, but at the price of a larger shift (-2 dB), as previously mentioned.

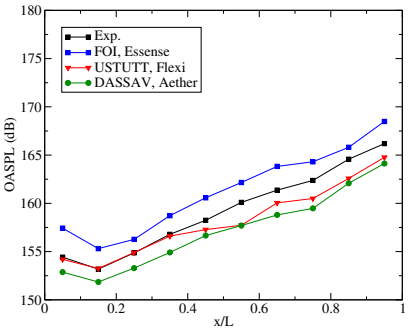

Fig. 10. Overall Sound Pressure Level (OASPL) using higher order methods (HO) by FOI-LiU, USTUTT, and DASSAV on the cavity ceiling (Kulites k20 - k29)

Next is a summary of the computational resources required to obtain the considered solutions. The reference calculation on the FOI grid has been left out. It should be noted that the simulation time is different for the calculations. The higher order simulation by FOI-LiU is obviously more than an order of magnitude more expensive than the FOI-LiU reference calculation. This is mainly due to small time steps and the lack of convergence acceleration in ESSENSE. The higher order calculation by USTUTT is more efficient and comparable to the reference solution by FOI. It is to be noted, that while the effective N_{DOF} is 7.7×10^6, the overall N_{DOF} including overintegration is about three times higher. DASSAV 3rd-order P2 simulations last about 2.5 times as long as a standard 2nd-order P1 simulation (6 days compared to 2.5 days on 1024 cores of an IBM BlueGene/P). Higher-order computations use 10 integration points per tetrahedron, whereas a single point is used for 2nd-order runs. It is quite possible that on this configuration where all elements have uncurved edges, a four-point integration rule would suffice, further reducing the cost of the higher-order simulation.

3 VALIANT Flap Case

The VALIANT flap testcase represents a wing+flap configuration in approach condition. This case is a generic geometry defined in the FP7 VALIANT project. The flap is placed under the wing with a bit of overlap. This configuration was installed in the anechoic wind tunnel of Ecole Central de Lyon and both flow and

Table 5. Computational information about the cavity test case

Partner/ case	Simulation time	N_{DOF}	N_{CPU}	T_{wall}	T_{bench}	$T_{wall} \times N_{CPU}/(T_{bench} \times N_{DOF})$
FOI-LIU HO	0.080 s	2.6×10^6	300	$7.70 \times 10^6 s$	16.0 s	56.00
FOI-LIU Ref.	0.200 s	6.2×10^6	64	$2.44 \times 10^6 s$	16.0 s	1.60
USTUTT HO	0.110 s	7.7×10^6	4096	$1.75 \times 10^5 s$	15.1 s	6.10
DASSAV Ref.	0.225 s	3.5×10^6	1024	$2.12 \times 10^5 s$	131.5 s	0.47
DASSAV HO	0.225 s	3.5×10^6	1024	$5.48 \times 10^5 s$	131.5 s	1.20

acoustic measurements were performed in the framework of VALIANT (VALidation and Improvement of Airframe Noise prediction Tools) FP-7 European project [13]. The main characteristics defining the flow are the free-stream velocity $U_{\inf} = 51 m/s$, which corresponds to approach condition with $Ma = 0.15$. The resulting Reynolds number, $Re = 1.36 \times 10^6$, is approximately one order of magnitude less than the Reynolds numbers corresponds to a real aircraft wing during approach. Roughness elements (sandpaper ISO P150) were placed on both sides of the wing in order to trigger an established incoming turbulent boundary layer. The experimental database obtained by ECL includes the following data: time-dependent microphone signals, time-dependent wall pressure signals, time-dependent series of the velocities acquired from hot wire measurements [14].

3.1 Computational Domains and Grids

As a first step towards the characterization of the noise propagation from this generic wing flap configuration, the computational domain of the LES simulation was extended for the LEE simulation. Acoustic measurement data are available 2 meters above the wing trailing edge, so this point was considered in the LEE domain to be resolved. The boundary of the computational domain, therefore, was truncated a bit further above this measurement point in order to limit the reflections arising due to this artificial domain restriction. The computational domain can be seen in Figure 11. This 2D mesh consists of 36k triangular elements, heavily clustered in the noise production region in order to have a good representation of the reconstructed source terms transferred from the LES simulation.

The maximum mesh size was determined based on the maximum frequency resolution we intended to achieve. Previous investigations showed that with P1 representation, the LDA scheme needs 10 points per wavelength. The maximum frequency resolution we can have from the LES source data can be computed as:

$$f = 1/\Delta t_{LES} = 1/10^{-6} = 10^3 kHz \tag{4}$$

Due to the space-time discretization, we need ten points in time, as well, to resolve the waves in time, giving the maximum assessable frequency of

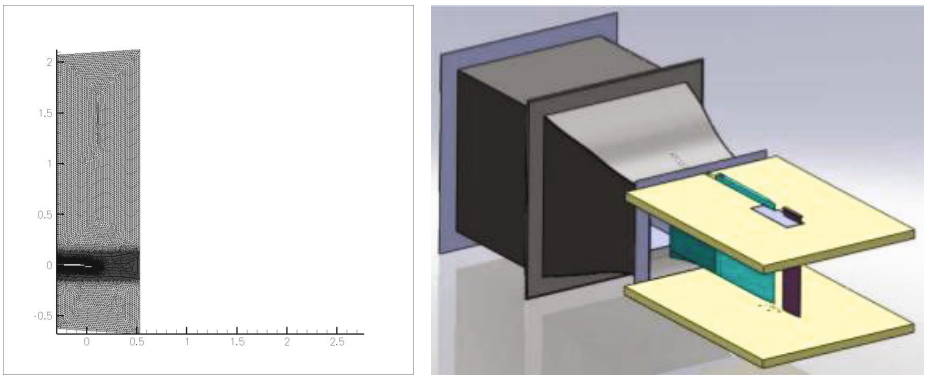

(a) Computational domain of VKI (b) Measurement setup

Fig. 11. Quasi-2D wing and flap configuration

$f_{max} = 10^2 kHz$. This frequency is still far above the maximum frequency of the measurements ($20kHz$), so we decided to limit the maximum frequency resolution to this value, giving the maximum cell size:

$$\Delta x = \frac{\lambda}{100} = 0.1\frac{c}{f} = 2mm \tag{5}$$

TsAGI performed calculations of this test as well in 2D (flat) formulation. 2D basis functions were used in DG method. Initially, RANS calculation has been performed on appropriate grid with detailed resolution of turbulent boundary layer (for uniform inflow). The converged flowfield, obtained in RANS calculation, have been used as basic (aerodynamic) flowfield.

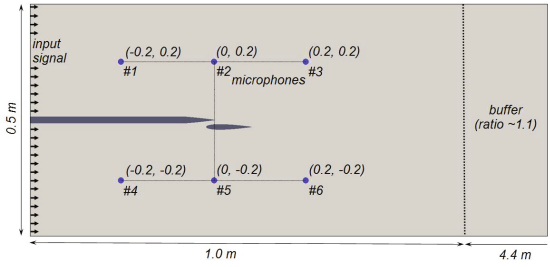

Fig. 12. Geometry of computational domain and position of control points for test A14 by TsAGI

Acoustic calculations have been performed using DG method $K = 3$ for four quasi-uniform grids with quasi-quadratic cells, with 4, 6, 9 and 14 cells per the shortest wavelength in the incoming sound. TsAGI used a smaller domain in order to be able to perform parametric studies and grid convergence.

3.2 Numerical Methods and Baseline Solutions

The von Karman Institute used their second- and third-order Residual Distribution solver to deal with this noise propagation problem. The Residual Distribution or Fluctuation Splitting Method is somewhere between the Finite Element and Finite Volume Methods. The idea was introduced in 1982 by P.L. Roe and later extended for the solution of conservation laws on unstructured meshes. In the last decades several multidimensional upwind schemes have been developed, and proved to be accurate and robust. A new strategy in the computation of the residuals has been designed involving contour integrations and leading to conservative discretization even for problems where it is not possible to linearize the system of equations. Thanks to this improvement the application of RDS to high order discretisation was possible. In our case, since we want to distribute to the downwind nodes it is necessary to split the high order elements in linear elements where we know how to use a multidimensional upwind distribution. Several methods have been developed to solve unsteady problems. In this work we used the space-time method, where the time is considered as a third dimension yielding a space-time element and was first presented by Ricchiuto et al. [15]

In the present work we consider the Linearized Euler Equations (LEE) in two spatial directions, as derived by Bailly et al. for inhomogeneous mean flow, written in conservative variables. At the boundaries non-reflective boundary conditions are used. This boundary treatment relies on the characteristic theory. It is well known that the number of physical conditions which has to be prescribed at the boundary depends on the sign of the eigenvalues of the characteristic system. Only the information coming from outside has to be imposed, all the others are provided naturally by the inner domain. In case of acoustic problems the first difficulty arising is to know what kind of conditions should be fixed. In the present Linearized Euler Equations, the solution variables are the fluctuations of density, velocity and pressure. At an inflow boundary condition three of them should be given, for an outflow just one. But none of the conservative variables are known, in general. It is much easier acting on the waves themselves.

In order to perform noise propagation simulation with the help of Linearized Euler Equations, the background flow (time-averaged) needs to be provided to the solver. VKI was using the time-averaged mean flow provided by the LES, extrapolated to the regions, what the LES domain do not cover. The non-uniform mean flow expected to effect the noise propagation, therefore its correct representation is an important step of the current procedure. The noise production calculation of the generic wing and flap configuration was set up and validated within the FP7 VALIANT project. This simulation was continued to collect equivalent noise sources for the LEE solver used for noise propagation simulation. The noise sources produced by the open source OpenFOAM solver were collected for a time span of $T = 0.04s$ and saved to be able to transfer them to our in house code COOLFluiD. In order to reduce the data amount of these volumetric sources, only the mid-span averaged data was extracted in every time-step.

Based on the incompressible flow quantities, equivalent acoustic sources were reconstructed as:

$$\mathbf{S} = \begin{bmatrix} 0 \\ S_i - \bar{S}_i \\ 0 \end{bmatrix} \tag{6}$$

where $S_i = -\frac{\partial \rho_0 u_i' u_j'}{\partial x_j}$. These source terms were directly used as volumetric source terms, but the source domain was truncated to a disk of 10cm around the wing trailing edge, where the dominant source terms are located, in order to reduce the numerical noise due to interpolation of the sources from the fine LES mesh to the coarser LEE mesh.

In the previously discussed manner the reconstructed sources from the LES simulation were introduced in the LEE simulation. A total simulation time of $T = 0.04s$ was covered by the propagation simulation limiting the statistically converged low frequency resolution to $f = 6kHz$. The effect of the non uniform flow is clearly visible in Figure 13, where the instantaneous divergence of velocity is plotted.

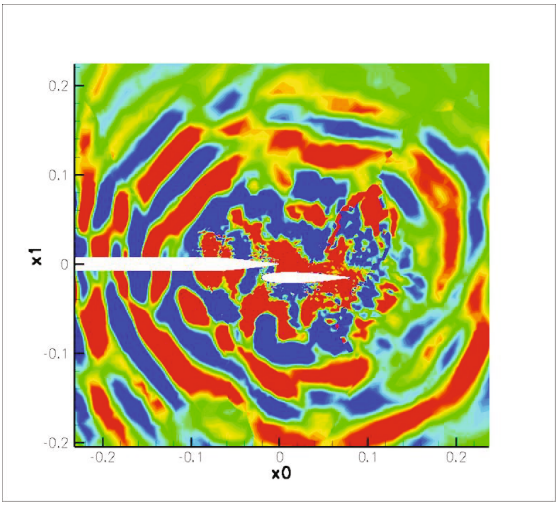

Fig. 13. Contours of divergence of velocity indicating the noise propagation pattern

In the present simulation, only spanwise averaged data were stored and a 2D propagation simulation was performed. According to Manoha *et al.* [16] only the zeroth spanwise wavenumber of the spanwise, Fourier-transformed source needs to be considered. Based on this observation Ewert *et al.* [17] used a reduced 2D source in a pure 2D acoustic simulation to correct the sound pressure levels from 2D to 3D. In the present case the method suggested by Ewert *et al.* is followed.

The integral length scale of the acoustic source in the spanwise direction is small compared to the acoustic wavelength for low Mach numbers, so the source

is compact in this direction. Therefore, an acoustic simulation with a spanwise extension L_z and periodic boundary conditions is equivalent to a 2D acoustic simulation with a spanwise averaged acoustic source [17]:

$$\widehat{s_x} = \frac{1}{L_z} \int_{-L_z/2}^{L_z/2} s_x dz \tag{7}$$

If these averaged source terms are used in a 2D acoustic simulation, the sound-pressure correction form 2D to 3D becomes:

$$\widehat{p}(0, R, \theta, \omega) \backsimeq \widehat{p}(R, \theta, \omega) \frac{1 - \imath}{2} \sqrt{\frac{k\Delta^2}{\pi R}} \tag{8}$$

where $\widehat{p}(0, R, \theta, \omega)$ denotes the 3D, $\widehat{p}(R, \theta, \omega)$ the 2D , frequency-related Fourier transform of the sound pressure, ω is the angular frequency and $k = \omega / c_0$ is the wavenumber. This correction affects the final SPL distribution, but has no impact on the θ-dependent directivity. The SPL correction based on Equation 8 is:

$$SPL_{3D,L_z} = SPL_{2D} + 10log\left(\frac{f\Delta^2}{Rc_0}\right) \tag{9}$$

So, the 2D sound-pressure spectrum is shifted 3 dB/octave towards the higher frequencies by the correction. The SPL_{3D,L_z} is the sound radiated by the slice of airfoil simulated by LES. For a finite spanwise extension L_{span} an additional correction is needed:

$$SPL_{3D,L_{span}} = SPL_{3D,L_z} + 10log\left(\frac{L_{span}}{\Delta}\right) \tag{10}$$

This correction is based on the assumption that all slices of L_z along the wingspan are uncorrelated, whereas the spanwise extension is small compared to the distance between the source and the listener (R).

There are several approaches for solving acoustic tasks. The approach, which was considered by TsAGI, is known as "perturbation method" [18]. It requires relatively not much computational costs and consists of three general steps. At the first step a basic aerodynamic flowfield is calculated independently using Reynolds averaged Navier-Stokes equations. Then near acoustic field is simulated directly as generation and propagation of small acoustic perturbations over the aerodynamic field. This direct numerical simulation of sound is performed on the basis of linearized Euler equations. And finally far acoustic field is estimated using special methods (Kirchhoff or Ffowcs-Williams Hawkings methods), which consider radiation of sound by control surface over practically uniform aerodynamic field. Acoustic characteristics of the control surface are taken from the calculation of near acoustic field. TsAGI work within IDIHOM project was concentrated on direct simulation of sound propagation in near acoustic field. Theoretically, it is possible to neglect the influence of viscosity on sound propagation and to consider this process as adiabatic. To minimize essentially the quantity of arithmetic operations, it was decided to calculate sound propagation on the basis

of Isentropic Linearized Euler Equations (ILEE). This equation system may be obtained from full linearized Euler equations, if we replace the last differential equation (for energy) by isentropic relation $p' = c_a^2 \rho'$, where c is speed of sound and index a corresponds to basic (aerodynamic) flow.

ILEE equation system may be represented in the following form:

$$\frac{\partial U'}{\partial t} + \frac{\partial F_i'\left(U', U_a\right)}{\partial x_i} = 0,$$

where

$$U' = \begin{pmatrix} U_0' \\ U_1' \\ U_2' \\ U_3' \end{pmatrix} = \begin{pmatrix} \rho' \\ \rho_a u' + \rho' u_a \\ \rho_a v' + \rho' v_a \\ \rho_a w' + \rho' w_a \end{pmatrix}, \quad F_i'\left(U', U_a\right) = \begin{pmatrix} U_i' \\ U_1' u_{ia} + \rho_a u_a u_i' + c_a^2 U_0' \delta_{i1} \\ U_2' u_{ia} + \rho_a v_a u_i' + c_a^2 U_0' \delta_{i2} \\ U_3' u_{ia} + \rho_a w_a u_i' + c_a^2 U_0' \delta_{i3} \end{pmatrix}.$$

Here Cartesian coordinates $x_1 = x$, $x_2 = y$, $x_3 = z$; velocity components of basic (aerodynamic) flow $u_{1a} = u_a$, $u_{2a} = v_a$, $u_{3a} = w_a$; velocity perturbations $u_1' = u'$, $u_2' = v'$, $u_3' = w'$.

To construct DG method, the vector of primitive variables $Q' = [\rho'; u'; v'; w']^{\mathrm{T}}$ in each cell of computational grid is represented as a linear combination of local polynomial basis functions $\varphi_j(\mathbf{x})$:

$$Q' = \sum_{j=1}^{K_f} q_j(t) \varphi_j(\mathbf{x}),$$

Polynomial basis functions with maximal degree K provide (theoretically) the accuracy order $K + 1$ in space.

Coefficients of this expansion, $q_j(t)$, are the main unknown values in DG method. Equation system for the determination of $q_j(t)$ may be represented as follows:

$$\sum_{j=1}^{K_f} \left(\int_{\Omega} \Gamma \varphi_i(\mathbf{x}) \varphi_j(\mathbf{x}) d\Omega \right) \frac{dq_j}{dt} + \oint_{\Sigma} F_k' n_k \varphi_i(\mathbf{x}) d\Sigma = \int_{\Omega} F_k' \frac{\partial \varphi_i}{\partial x_k} d\Omega, \quad i = 1, \ldots, K_f.$$

Here Ω is volume of computational grid, Σ is its surface, $\mathbf{n} = [n_1; n_2; n_3]^{\mathrm{T}}$ is unit outer normal vector to the surface element $d\Sigma$, $\Gamma = \partial U'/\partial Q'$. This set of ordinary differential equations is solved using explicit four-stage Runge-Kutta method that can be described by Butcher tableau

Fluxes at the cell faces F_k' are calculated using Roe linearized solution of Riemann problem about the decay of discontinuity between two flows adjoining to current point of cell surface. Approximate Roe matrix is used; it coincides with Jacobian of ILEE, computed using arithmetic averages of aerodynamic flows from two sides of the cell face.

Numerical experiments with 1D propagation of sine wave show that DG method with $K = 3$ allows to calculate propagation of sound waves on grids with only 3 cells per wavelength.

0	
1/4	1
1/3	0 1
1/2	0 0 1
	0 0 0 1

3.3 Assessment of High-Order Solutions

The final comparison with the measurements in the measurement location 2m above the wing trailing edge can be seen in Figure 4. Both P1 and P2 results are represented in this graph. The comparison shows a good agreement both for P1 and P2 discretization. In our RDS code the P2 discretozation was not giving significant improvement, but increased the simulation time. Thanks to the good performance of the P1 element (10 point/wavelength) the P2 discretization do not have a lot of room of improvement. Though, it must be stressed, that the P2 discretization can catch the wave propagation speed a bit better, since it introduces less dispersion error, than the P1 element.

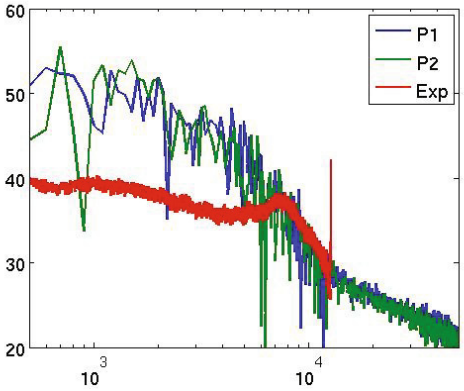

Fig. 14. LEE simulation compared with experimental data

In the main series of calculations by TsAGI, stochastic perturbations were continuously introduced from the inflow boundary. Stochastic perturbations with nearly uniform flat distribution (in 1/3rd octave presentation) within the frequency range 100-12000 Hz were used. Instant field of pressure perturbations in the time moment $t = 0.00615s$ is shown in Figure 15. One may see that incoming sound waves propagate (practically without damping) along the computational domain. Their diffraction and reflection from the flap tip may be seen.

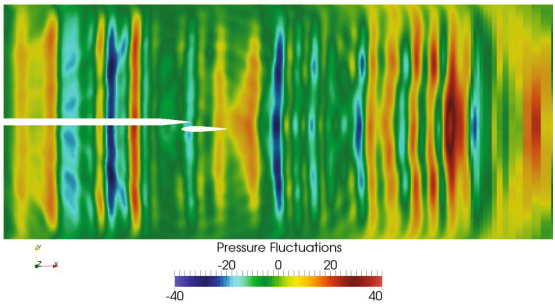

Fig. 15. Instant field of pressure fluctuations in the case of stochastic perturbations at the inflow

After that, an attempt has been made to estimate the convergence order using the same procedure as in test with 1D propagation of a sine wave. Dependencies were registered in six control points that are shown in Figure 12. RMS value of pressure perturbations was determined. Using sequences of for 3 grids, convergence order has been estimated. But this attempt has appeared to be unsuccessful. In some points the convergence order was undetermined, in other points it was far from the expected values, and in different points these values were very different.

To understand this result, additional series of calculation have been performed. Now the flat sine waves of maximal frequency (12000 Hz) were introduced continuously through the left boundary. Maximal frequency was chosen to have the maximal approximation errors and to avoid the influence of truncation errors on the results of Richardson extrapolation. Instant field of pressure perturbations in the same time moment is shown in Figure 16. Attempt to estimate the convergence order has been performed again. And it appeared to be unsuccessful, too. Analysis of Figure 6 allows to assume that the reason of the unsuccess in the convergence order determination is the interference of the main flat waves (propagating to the left) with the waves, reflected from the flap tip and from the upper or lower boundaries of computational domain. Even if all

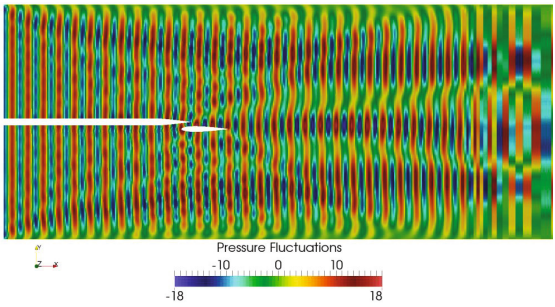

Fig. 16. Instant field of pressure fluctuations in the case of monochrome sinusoidal perturbations at the inflow

these waves have the same frequency, the behavior of signal in control points depends not only upon the grid resolution but also upon the phase shift between the interfering waves. It is important to note that in a test with 1D propagation of the same sine wave on comparable grids the convergence order is determined successfully; it appears to be close to the expected value −4.

4 Conclusion

For the cavity test case higher order accurate solutions over the cavity have been provided by FOI-LIU, USTUTT, and DASSAV. The quality of the solutions is good in terms of SPL and OASPL with similar quality as obtained by a reference solution with about the same number of degrees of freedom. The flow physics are well captured in both the reference and higher order accurate solutions. The computational costs for the higher order results are somewhat higher than those of the reference solution. Further calculations and comparisons on somewhat coarser grids would be needed to judge if the higher order computations pay off compared to a reference solution.

The baseline simulation of the VALIANT testcase showed the potential of hybrid LES/LEE method for noise propagation. The procedure starts with a high fidelity Large-Eddy Simulation in the noise propagation region. After statistical convergence is reached, instantaneous volumetric/spanwise averaged noise sources can be extracted. These sources then introduced to the Linearized Euler Equation solver in order to simulate noise propagation for larger distances. With a high fidelity computation this would be impossible due to the associated high computational cost.

The bottleneck of the procedure is the data transfer between the two solvers. This requires a huge amount of data to be written by the LES solver and read by the LEE solver. Even in the case of the 3D LES to 2D LEE it meant several Gb storage and file I/O. In order to overcome this limitation, it is recommended that the two set of equations are solved simultaneously and the source terms are transferred directly between the solvers.

It was shown that in case of our Residual Distribution solver, the P1 and P2 discretization gave the same quality in terms of noise prediction. For this study two meshes with approximately the same degree of freedom was generated. Though, the P2 simulation took 6 times longer than the P1 (48 CPU hour / 0.001s simulation time for the P1). As a onclusion, the higher order method we are using clearly has higher accuracy for academic cases, but is not justifiable for industrial usage.

Explicit high-order Discontinuous Galerkin method (K=2-3) is implemented for solution of unsteady Isentropic Linearized Euler equations for solution of aeroacoustical tasks by TsAGI. Method with K=3 allows to calculate propagation of sound waves on grids with only 3 cells per wavelength. Grid convergence order of the method is close to the expected value , if tasks without interference of waves with different frequency and phase shift are considered. In task with interference of waves, standard approach to determination of the convergence order seems to be inapplicable.

References

1. Chen, X., Sandham, N.D., Zhang, X.: Cavity Flow Noise Predictions, Report No. AFM-07/05, School of Engineering Sciences, University of Southampton (2007)
2. Ashworth, R.M.: Prediction of acoustic resonance phenomena for weapon bays using detached eddy simulation. Aeronautical Journal, 631–638 (2005)
3. Peng, S.-H.: Simulation of Flow Past a Rectangular Open Cavity using DES and unsteady RANS, AIAA Paper 2006-2827 (2006)
4. Eliasson, P., Weinerfelt, P.: Recent Applications of the Flow Solver Edge. In: Proceedings to 7th Asian CFD Conference, Bangalore, India (2007)
5. Sørensen, K.A., Johnston, C., Leicht, T., Chalot, F., Eliasson, P., Bassi, F., Couaillier, V., Kessler, M.: External Aerodynamic Test Cases. In: Kroll, N., Hirsch, C., Bassi, F., Johnston, C., Hillewaert, K. (eds.) IDIHOM: Industrialization of High-Order Methods - A Top-Down Approach. NNFM, vol. 128, pp. 559–614. Springer, Heidelberg (2015)
6. Chalot, F., Dagrau, F., Mallet, M., Normand, P.E., Yser, P.: Higher-order RANS and DES in an industrial stabilized finite element code. In: Kroll, N., Hirsch, C., Bassi, F., Johnston, C., Hillewaert, K. (eds.) IDIHOM: Industrialization of High-Order Methods - A Top-Down Approach. NNFM, vol. 128, pp. 495–525. Springer, Heidelberg (2015)
7. Nordström, J., Gong, J., van der Weide, E., Svärd, M.: A Stable and Conservative High Order Multi-block Method for the Compressible Navier-Stokes Equations. Journal of Computational Physics 228, 9020–9035 (2009)
8. Berg, J., Nordström, J.: Stable Robin Solid Wall Boundary Conditions for the Navier-Stokes Equations. Journal of Computational Physics 230, 7519–7532 (2011)
9. Taube, A., Munz, C.D.: Test Case Report CTC 1 Cavity. ADIGMA project report (2009)
10. Hindenlang, F., Gassner, G., Altmann, C., Beck, A., Staudenmaier, M., Munz, C.-D.: Explicit discontinuous Galerkin methods for unsteady problems. Computers & Fluids 61, 86–93 (2012)
11. Deck, S.: Recent improvements in the Zonal Detached Eddy Simulation (ZDES) formulation. Theor. Comput. Fluid. Dyn. 26, 523–550 (2012)
12. Larchevêque, L., Sagaut, P., Lê, T.-H., Comte, P.: Large-Eddy Simulation of a compressible flow in a three-dimensional open cavity at high Reynolds number. Journal of Fluid Mechanics 516, 265–301 (2004)
13. `http://www.cimne.com/websasp/valiant/`
14. Lemoine, B., Roger, M., Legriffon, I.: Aeroacoustics of a Model Non-Lifting Wing-Flap System in a Parallel Flow. In: 17th AIAA/CEAS Aeroacoustics Conference, Portland OR, June 6-8, pp. 2011–2735. AIAA paper 2011-2735 (2011)
15. Ricchiuto, M., Csik, A., Deconinck, H.: Residual distribution for general time dependent conservation laws. J. Comput. Phys. 209, 249–289 (2005)
16. Manoha, E., Delahay, C., Ben Khelil, S., Guillen, P., Sagaut, P., Mary, Y.: Numerical prediction of the unsteady flow and radiated noise from a 3d lifting airfoil. AIAA 2001-2133 (2001)
17. Ewert, R.: Acoustic perturbation equations based on flow decomposition via source filtering. J. of Comp. Physics 188 (2003)
18. Vlasenko, V., Bosniakov, S., Mikhailov, S., Morozov, A., Troshin, A.: Computational approach for investigation of thrust and acoustic performances of present-day nozzles. In: Progress in Aerospace Sciences, vol. 46, pp. 141–197 (2010)